Earth, Planets and Space
a SpringerOpen Journal

FULL PAPER

Open Access

CrossMark

Observations of stratospheric and mesospheric O_3 with a millimeter-wave radiometer at Rikubetsu, Japan

Hirofumi Ohyama[1*], Tomoo Nagahama[1], Akira Mizuno[1], Hideaki Nakane[2,3] and Hideo Ogawa[4]

Abstract

We have been measuring brightness temperature spectra of the atmospheric ozone (O_3) emission at 110.83 GHz with a millimeter-wave radiometer (MWR) located at Rikubetsu, Japan, since November 1999. Tropospheric opacities, which were also measured with the MWR and were used to take into account attenuation of the O_3 signal from the stratosphere and mesosphere, were corrected using the tropospheric opacity calculated from radiosonde data. Temporal variations of the measured spectral intensity of O_3, likely due to degradations of the superconductor–insulator–superconductor receiver and of the vessel for cold calibration load, were also corrected using scaling factors derived from ozonesonde data up to an average height of 35 km and Microwave Limb Sounder (MLS) monthly mean climatology above the sonde height. The vertical profiles of the O_3 mixing ratio in the altitude range from 24 to 56 km were retrieved from the spectra with the optimal estimation approach. The retrieval errors from uncertainties in the scaling factor, the corrected tropospheric opacity, and atmospheric temperature, as well as those from spectral noise, were evaluated, and we found that the main retrieval errors resulted from uncertainties in the scaling factor and tropospheric opacity. The retrieved O_3 profiles were compared with those from the Solar Backscatter Ultraviolet (SBUV/2), the Sounding of the Atmosphere using Broadband Emission Radiometry (SABER), and the MLS instruments onboard satellites. The retrieved O_3 mixing ratios at individual levels agreed with the MLS version 3.3 or 3.4 data with an average difference better than ± 5 % and a standard deviation of 4–9 %. Additionally, the retrieved O_3 profiles were in reasonable agreement with the SABER version 2.0 O_3 profiles and the SBUV/2 version 8.6 O_3 profiles, in line with the validation results of their satellite data in the earlier literature.

Keywords: Ozone, Remote sensing, Millimeter-wave radiometer, Retrieval

Background

Stratospheric ozone (O_3) plays an important role in protecting life on the Earth from solar ultraviolet radiation. Chlorine radicals, which are released mainly in the stratosphere by photodissociation of chlorine compounds, destroy O_3 in a catalytic cycle (Rowland and Molina 1975; Solomon 1999). According to the regulation of the emission of anthropogenic chlorine compounds, signs of slowdown in the decline of O_3 were reported in the upper stratosphere (Newchurch et al. 2003), and a positive

trend of about 4 % per decade in the upper stratosphere in the northern mid-latitudes has recently been found (WMO 2014). However, because the global distribution of stratospheric O_3 is affected by many factors, such as the trend of ozone-depleting substances, stratospheric temperature change due to global warming, and modulation of the Brewer–Dobson circulation, it is essential to continually observe the stratospheric O_3 abundance.

In order to monitor the depletion or recovery of stratospheric O_3 and to understand the chemical and dynamical processes controlling the O_3 trends, vertical distributions of various minor constituents, including O_3, have been measured with ground- and space-based instruments. A millimeter-wave radiometer (MWR) enables the continuous measurement of the atmospheric

*Correspondence: hohyama@stelab.nagoya-u.ac.jp
[1] Institute for Space-Earth Environmental Research, Nagoya University, Furo-cho, Chikusa-ku, Nagoya 464-8601, Japan
Full list of author information is available at the end of the article

Springer

Ohyama *et al. Earth, Planets and Space* (2016) 68:34

Page 2 of 14

constituents distributed from the middle stratosphere to the lower mesosphere, irrespective of day or night with a high temporal resolution of ~1 h, because it records an emission spectrum caused by the rotational transition of the atmospheric constituents. Such ground-based MWR measurements have been carried out at more than a dozen sites in the past decades (e.g., Daae et al. 2014; Fiorucci et al. 2013; Palm et al. 2010; Parrish et al. 2014; Schneider et al. 2003; Studer et al. 2012).

To investigate the various temporal variations of the middle atmospheric O_3 in the northern mid-latitude region, particularly in the Asian area, a ground-based MWR was installed at Rikubetsu (43.46°N, 143.77°E, 361 m above sea level), Japan, in March 1999. The National Institute for Environmental Studies (NIES) operated the MWR until March 2011, but subsequently the Institute for Space-Earth Environmental Research (ISEE) of Nagoya University has been responsible for its operation. The Rikubetsu site is a part of the Network for Detection of Atmospheric Composition Change (NDACC) (http://www.ndsc.ncep.noaa.gov/). The instrument has been tuned to the frequency of 110.836 GHz to observe the $6_{1,5}$–$6_{0,6}$ transition of O_3. Nagahama et al. (2007) reported O_3 observation at Rikubetsu with this instrument during the period from November 1999 to June 2002.

In the present study, the observation period was expanded to May 2014, a period during which the receiver and the spectrometer were replaced twice and the calibration method of the spectral intensity was changed. In the analysis of the longer time series data, we find that tropospheric opacity measured with the MWR as well as the brightness temperature of the O_3 emission spectrum varied with an unnatural trend. This was likely due to a degradation of the receiver and a defect in measuring the cold calibration load, and we were able to address these instrumental problems, as described in next section. In addition, we developed correction methods for the data already acquired, and the atmospheric O_3 profiles between approximately 24 and 56 km during the period from November 1999 to May 2014 were derived from the corrected spectra and tropospheric opacities. We note that the correction method of the brightness temperature was based on ozonesonde and Microwave Limb Sounder (MLS) data rather than properties on the MWR itself and that our data added information on continuous O_3 concentration variations with a temporal resolution of 1 h at a certain site to the ozonesonde/MLS measurements. To evaluate the accuracy of the retrieved O_3 profiles, the profiles were compared with O_3 profiles from the Solar Backscatter Ultraviolet (SBUV/2) instrument onboard the NOAA 11, 16, and 18 satellites (Bhartia et al. 2013), the Sounding of the Atmosphere using Broadband Emission Radiometry (SABER) instrument onboard the Thermosphere Ionosphere Mesosphere Energetics Dynamics satellite (http://saber.gats-inc.com/data.php), and the MLS instrument onboard the Aura satellite (Livesey et al. 2011).

Methods

Instrument and observation

The Rikubetsu MWR has a heterodyne receiver employing a superconductor–insulator–superconductor (SIS) mixer to convert the atmospheric O_3 signal down to that in an intermediate frequency range. The operation timeline of the instrument is listed in Table 1. The details of the instrument until October 2005 are described in Nagahama et al. (2007), and we present the changes that were made after October 2005. As for the receiver, a tunable SIS mixer was replaced with a sideband-separating SIS mixer (2SB mixer) made of two double sideband (DSB) mixers and two 90° hybrid couplers (Asayama et al. 2004) in October 2005. The 2SB mixer receiver was operated with a receiver noise temperature of 130–170 K in single sideband (SSB) mode, and the response of the image sideband was suppressed by up to 13 dB compared with that of the signal sideband. For the spectrometer, the bandwidth of the acousto-optical spectrometer (AOS) was changed from 0.5 to 1 GHz, but the number of channels remained unchanged (2048 channels). Although a hot blackbody, a cold blackbody, and a (low-angle) sky spectrum had been acquired in turn until October 2005, another sky spectrum with an elevation angle fixed at 70° was added to the observation sequence; this is referred to as the high-angle sky spectrum. Figure 1 shows a block diagram of the MWR after October 2005. A lossy dielectric plate is inserted in the high-angle sky spectrum observation to equalize the continuum levels of the high- and low-angle sky spectra. Because the continuum levels vary with time as the sky condition changes, the elevation angle of the low-angle sky spectrum is automatically adjusted so that the continuum levels of the high- and low-angle sky spectra are balanced (Mizuno et al. 2002; Parrish et al. 1988). The variable elevation angles can range from 12° to 45°. The rotating mirror looks toward the four directions with a measurement time of 3 s at each position. This cycle is repeated until the total measurement time at each position is 75 s (i.e., 25 cycles), and the average data for each target are recorded in a file. It takes approximately 9 min (including dead time for mirror switching) to acquire one spectrum. Here, the observed spectrum in brightness temperature T_{obs} is obtained as the difference between the low-angle sky spectrum T_{low} and the high-angle sky spectrum T_{high}, assuming a linear behavior among the sky, hot blackbody, and cold blackbody measurements:

Ohyama *et al. Earth, Planets and Space* (2016) 68:34

Page 3 of 14

Table 1 Timeline of millimeter-wave radiometer at Rikubetsu

Period	SIS mixer	Spectrometer (bandwidth, resolution)	Target	Cold-load vessel
Nov 1, 1999–Sep 28, 2005	Tunable SSB mixer	AOS (0.5 GHz, 244 kHz)	Low-angle sky Hot- and cold-load	Polystyrene
Oct 27, 2005–Nov 19, 2008	2SB mixer	AOS (1 GHz, 505 kHz)	Low- and high-angle sky Hot- and cold-load	Polystyrene
Nov 25 2008–Jul 25, 2013	2SB mixer	AOS (1 GHz, 505 kHz)	Low- and high-angle sky Hot- and cold-load	Glass dewar
Sep 1, 2013–Dec 14, 2013	DSB mixer + sideband removal filter	AOS (1 GHz, 505 kHz)	Low- and high-angle sky Hot- and cold-load	Glass dewar
Since Dec 15, 2013	DSB mixer + sideband removal filter	Digital FFTS (1 GHz, 61 kHz)	Low- and high-angle sky Hot- and cold-load	Glass dewar

Fig. 1 Block diagram of the millimeter-wave radiometer (MWR) at Rikubetsu
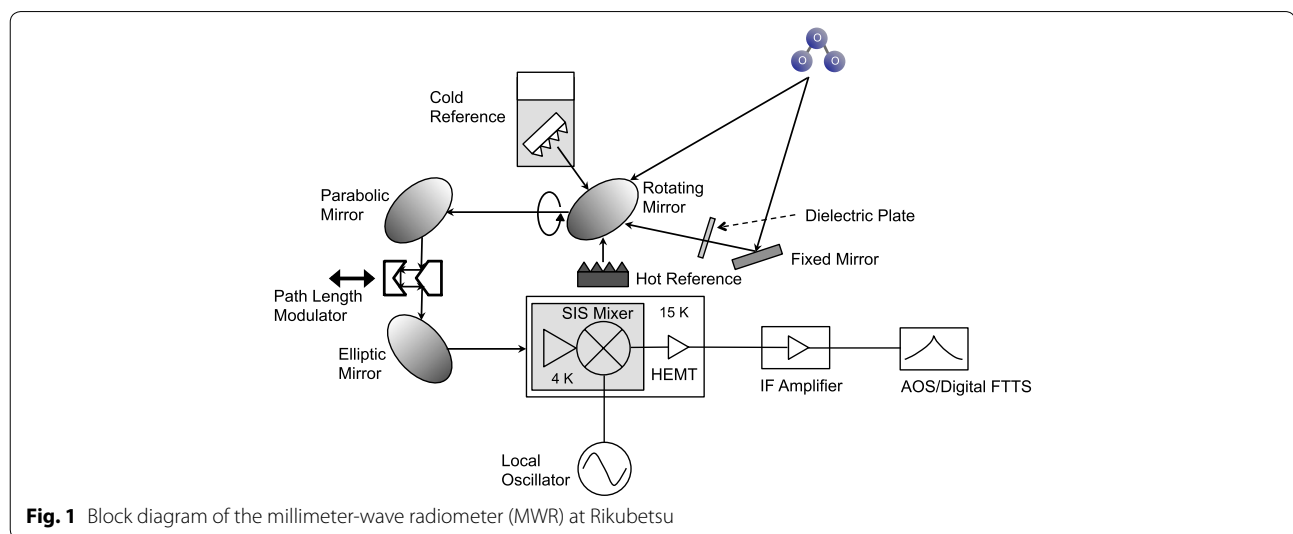
$$T_{\text{obs}} = T_{\text{low}} - T_{\text{high}} = \frac{T_{\text{hot}} - T_{\text{cold}}}{V_{\text{hot}} - V_{\text{cold}}}(V_{\text{low}} - V_{\text{high}}),$$

(1)

where V_{low}, V_{high}, V_{hot}, and V_{cold} are output from low-angle sky, high-angle sky, hot blackbody, and cold blackbody, respectively, and T_{hot} and T_{cold} are a hot blackbody (ambient) temperature and a cold blackbody (liquid nitrogen) temperature, respectively. The difference between the outputs from low- and high-angle sky is taken in order to remove a common spectral artifact and to suppress nonlinearity in the receiver system.

In 2013, a further modification was carried out with respect to the SIS mixer and the spectrometer. The degradation of the 2SB mixer became noticeable, as described in the next subsection, and we replaced the 2SB mixer with a sideband-separating mixer that consists of a DSB mixer and a sideband removal waveguide filter (Asayama et al. in preparation). In order to achieve higher spectral resolution measurements as well as to increase

stability against ambient temperature change, the AOS was replaced with a digital fast Fourier transform spectrometer (FFTS), which has a bandwidth of 1 GHz and a frequency resolution of 67 kHz. The hot and cold blackbodies are measured for 2 and 5 s, respectively, and subsequently, the low-angle and high-angle sky measurements of each 3 s are repeated 5 times. It takes approximately 1 min to complete this one cycle, and the data every one cycle are recorded in a file.

To correct an attenuation of the O_3 signal in the troposphere, which is attributed to absorptions by discrete oxygen (O_2) and water vapor (H_2O) lines and the H_2O continuum, their tropospheric opacity is derived based on the "sky-tipping" procedure (Ulich et al. 1980; Kuwahara et al. 2012). The sky-tipping procedure was executed every ~9 min before December 14, 2013, and is executed every ~8 min after that, requiring ~40 s to complete the one procedure. For O_3 retrieval, we make the hourly spectrum as follows. We select O_3 spectra which have elevation angles between 15° and 40° and tropospheric

Ohyama *et al. Earth, Planets and Space* (2016) 68:34

Page 4 of 14

opacity between 0.05 and 0.40 and calculate their average elevation angle and tropospheric opacity. Provided that the respective elevation angles are within ±1.0° of the average elevation angle and the tropospheric opacities are within ±0.05 of the average tropospheric opacity, the corresponding spectra are employed for calculating the hourly averaged spectrum.

Data corrections

During the observing period discussed in this paper, the measured tropospheric opacity and brightness temperature of the O_3 emission spectrum varied significantly probably due to the following two causes:

1. The 2SB mixer, which had been employed between October 2005 and September 2013, degraded, particularly after June 2009.
2. Until November 2008, the spectral intensity of the cold blackbody had a large uncertainty. The cold blackbody as a calibration source was placed inside a polystyrene vessel filled with liquid nitrogen, and its signal was measured through the polystyrene wall because of the high transmittance of the polystyrene in the millimeter-wave region. However, the polystyrene absorbs atmospheric moisture, particularly in the summer season, and the transmittance deteriorates. Even though we replaced the polystyrene a few times each year, the polystyrene that had absorbed atmospheric moisture affected the measurements of tropospheric opacity and brightness temperature.

After November 2008, the cold blackbody was placed inside a glass Dewar, and its signal was measured directly from above the Dewar using several mirrors. In addition, the 2SB mixer was replaced with the sideband-separating mixer in September 2013. For the data obtained before then, we developed methods for correcting the tropospheric opacity and spectral intensity.

First, the tropospheric opacities were calculated from semidiurnal radiosonde profiles launched at stations as much as possible near Rikubetsu, provided that the radiosonde launch time was within ±30 min of the average measurement time of the MWR hourly spectrum. The radiosonde data were obtained from the Integrated Global Radiosonde Archive (Durre et al. 2006). Because the radiosonde observation at Nemuro (43.33°N, 145.58°E, about 150 km from Rikubetsu), which is the nearest station to the Rikubetsu Observatory, discontinued in March 2008, the radiosonde profiles at Sapporo (43.05°N, 141.33°E, about 200 km from Rikubetsu) were used for the rest of the time. To be comparable to the measured opacity, the calculations of the opacity were implemented using the radiosonde data above 370 m

(i.e., height of the MWR instrument). For the calculation of the opacity, the Van-Vleck-Weisskopf function (1947) was used as the line profile function for H_2O and O_2. Spectroscopic line parameters for H_2O were taken from the HITRAN 2012 database (Rothman et al. 2013), whereas those for O_2 were taken from the line parameter files provided by Atmospheric and Environmental Research, Inc (AER: http://rtweb.aer.com/), which include first-order line-mixing coefficients at four specific temperatures (Tretyakov et al. 2005). Continuum absorptions due to H_2O were calculated using version 2.5.2 of the MT CKD continuum model (Mlawer et al. 2012) from the AER. Figure 2 shows time series of the measured and calculated tropospheric opacities and their percentage differences. The monthly mean differences are also shown, and they range from −50 to 40 %. Here, in order to investigate the effect of the change in the radiosonde launch site, the opacities from the Sapporo radiosonde data before March 2008 were also calculated (not shown). Although the individual differences in the opacities between Nemuro and Sapporo were up to ~100 % due likely to spatial variability of H_2O, the monthly mean differences in the opacities were less than 15 % (i.e., smaller than bias in the measured opacity) since the spatial variability was decreased by taking the monthly mean. Therefore, if the monthly mean value of the differences between the measured and the calculated opacities was used for the correction of the measured opacity, the effects of the change in the radiosonde launch site as well as of the spatial variability of H_2O between the MWR and radiosonde launch sites could be significantly reduced. Thus, the individual measured opacity was corrected on the basis of the monthly mean value of the percentage differences between the measured and the calculated opacities. We note that if the number of matchup data between the measured and the calculated opacities in one month was less than 10, the monthly mean value was replaced by the value of the previous month.

Second, we developed a procedure for correcting the brightness temperature of the O_3 emission line, in which we used three independent measurement datasets of O_3: Ozonesonde profiles observed approximately once a week at Sapporo and archived at the World Ozone and Ultraviolet Radiation Data Center (WOUDC) by the Japan Meteorological Agency, O_3 profiles from the MLS, and total O_3 columns from a Brewer spectrophotometer operated by the NIES at the Rikubetsu Observatory.

1. Ozonesonde profiles measured up to altitudes of at least 26 km were selected, and the average sonde height was approximately 35 km.
2. For the ozonesonde profile data, we applied a new correction factor that was recalculated according

Ohyama *et al. Earth, Planets and Space* (2016) 68:34

Page 5 of 14
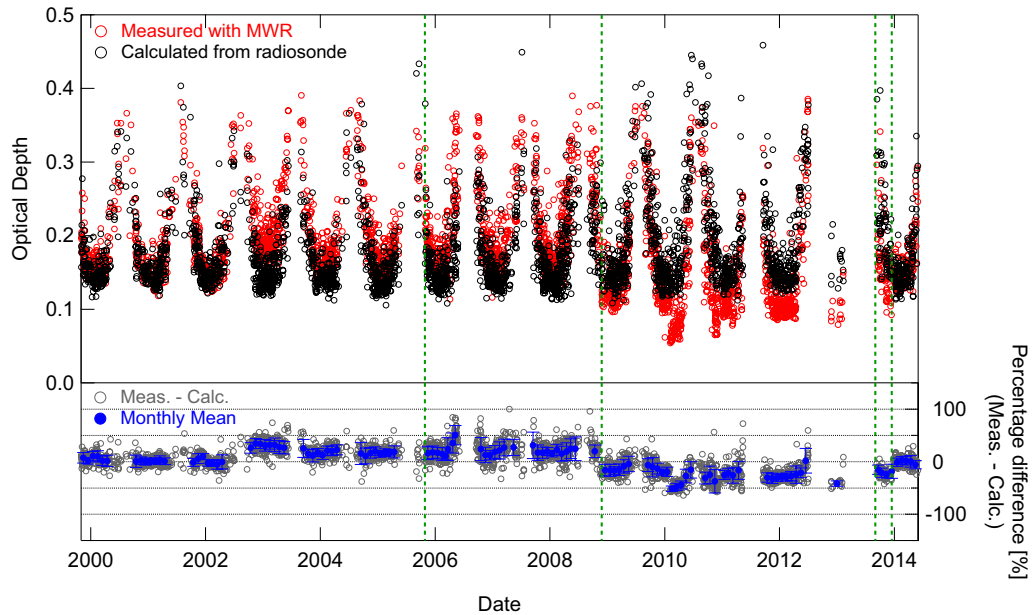
Fig. 2 Time series of tropospheric opacities from the MWR and radiosonde data. *Black* and *red open circles* indicate the tropospheric opacities calculated from the radiosonde data and those measured with the MWR within ±30 min of the radiosonde observation, respectively. *Gray open circles* are the differences between the measured and calculated tropospheric opacities, and *blue closed circles* and *error bars* denote the monthly mean differences and their standard deviations (±1σ), respectively. *Green dash lines* indicate the times of the change in the instrumentation described in Table 1

to the approach described in Morris et al. (2013), instead of the correction factor included in the WOUDC file.

3. Each ozonesonde profile with the new correction factor applied was complemented by the O_3 climatology profile above the balloon burst height. The O_3 climatology profiles were made per month by averaging the O_3 profiles and geopotential heights from the MLS observations between 2005 and 2013 (Livesey et al. 2011) within a ±5° latitude and ±15° longitude box centered on Rikubetsu. The climatological monthly profiles were produced separately for daytime (solar zenith angle (SZA) ≤ 98°) and nighttime (SZA > 98°) data. The O_3 concentrations above the balloon burst height were provided by linearly interpolating in time the daytime climatology profiles arranged at the middle of each month. Note that since the ozonesonde observations at Sapporo were limited to daytime, only the daytime climatology was used here. If the total O_3 column derived from the ozonesonde profile complemented by the climatology did not agree to within ±15 % with those derived from the Brewer spectrophotometer at Rikubetsu, we considered that the two instruments observed a different air mass and the ozonesonde data were not used.

4. A synthetic spectrum was calculated from the ozonesonde profile complemented by the climatology, according to a radiative transfer theory using the Voigt function as the O_3 line profile. The O_3 line intensity for a single molecule and the center frequency were taken from the Jet Propulsion Laboratory catalog (http://spec.jpl.nasa.gov/ftp/pub/catalog/catform.html) (Pickett et al. 1998), and other spectroscopic parameters were obtained from the HITRAN 2012 database (Rothman et al. 2013). Pressure and temperature profiles were calculated by connecting the National Centers for Environmental Prediction reanalysis data up to ~30 km (Kalnay et al. 1996) with the COSPAR international reference atmosphere data (Fleming et al. 1990). As the observed spectrum was created from the bidirectional spectra (low- and high-angle sky spectra), as given by Eq. (1), a comparable spectrum T_{calc} was calculated in the forward model:

$$T_{calc} = (T_{low} + T_{bg}e^{-m_{low}\tau_{ozone}})e^{-m_{low}\tau_z} \\ - (T_{high} + T_{bg}e^{-m_{high}\tau_{ozone}})e^{-m_{high}\tau_z - \tau_d}, \quad (2)$$

where T_{low} and T_{high} are the brightness temperature spectra calculated for the low- and high-angle sky directions, respectively, T_{bg} is the brightness

Ohyama *et al. Earth, Planets and Space* (2016) 68:34

Page 6 of 14

temperature of the cosmic background radiation, m_{low} and m_{high} are air-mass factors for the low- and high-angle sky directions, respectively, and τ_z, τ_d, and τ_{ozone} are optical depths of the lower atmosphere for the zenith direction, of the lossy dielectric plate, and of the O_3 integrated toward the zenith direction, respectively. The spectral baseline was represented by a first-order polynomial.

5. A factor was determined to minimize the difference between the synthetic spectrum multiplied by the factor and the observed spectrum, along with offset and slope for the baseline polynomial by the least squares method. Although the spectral range between 110.70 and 110.98 GHz was used, the spectral range within $\pm 1.6 \times 10^{-3}$ GHz from the line center was not used because the spectral range includes mostly information on the mesospheric O_3 concentration, whose uncertainty in the climatology might be large. The retrieved factor is hereafter called the "scaling factor." The scaling factors were derived from the MWR spectra within ± 3 h of the ozonesonde measurement time, and then the average value within ± 3 h (i.e., average of at most 6 data) was calculated. The scaling factor from one ozonesonde measurement to another was assumed to vary linearly in time, and the value for each MWR spectrum was derived by linear interpolation.

6. The observed spectrum was divided by the scaling factor.

Figure 3 shows time series of the retrieved scaling factor. Alternate scaling factors, which were obtained from each spectrum by using the MLS climatology over all altitude ranges instead of the ozonesonde, are also shown. The scaling factors derived from only the MLS climatology were not actually used for correcting the measured spectrum, but used for data screening as described in the subsequent section. Taking into account the accuracy of ozonesonde data of 5–10 % (Smit et al. 2007) and the temporal and spatial variability of the complemented O_3 climatology, the error upper limit of the scaling factor was estimated by shifting the O_3 profile by ± 20 % over all altitude ranges. We found that the change of the scaling factor was almost proportional to that of the O_3 profile [i.e., the retrieved scaling factors were estimated to have an error of ± 20 % (3σ)]. The retrieved scaling factors range from 0.4 to 1.6 and have large variability compared to the estimated error of the scaling factor. The large values in the summer seasons until the year 2006 may be attributable to degradations of the vessel for cold calibration load. Although the old cold load was still in use in 2007 and 2008 summer, the scaling factors during the periods were relatively stable because we frequently replaced the polystyrene vessel to new one. The low values after February 2011 may be due to degradation of the SIS receiver. When the receiver was replaced in September 2013, as described above, the values were close to 1.0.

Retrieval analysis

For the O_3 profile retrieval, an optimal estimation scheme (Rodgers 2000) was adopted. The retrieval algorithm employed in the present study was based on that described in Ohyama et al. (2012), which has been
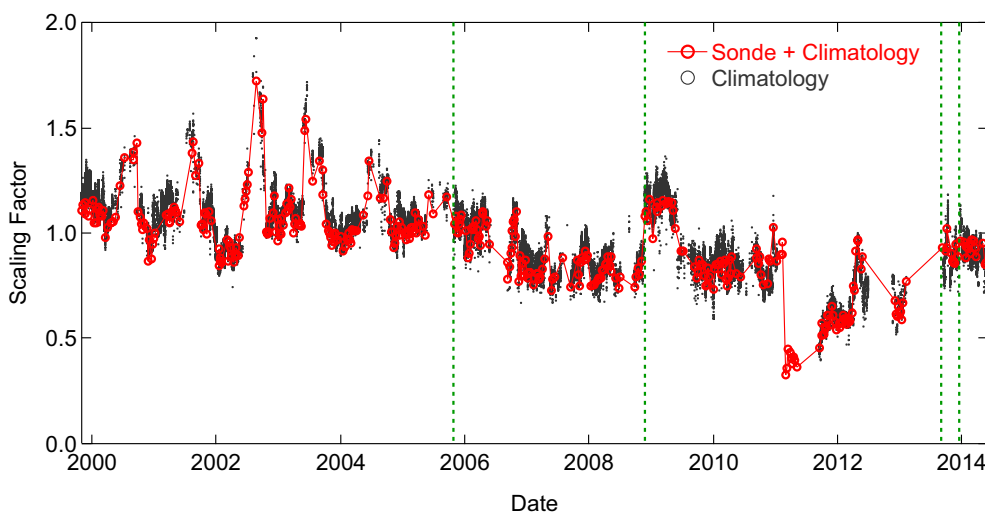
Fig. 3 Time series of scaling factors for correcting spectral intensity. The scaling factors are derived from the ozonesonde profiles up to the balloon burst height (at least 26 km) and MLS monthly mean climatology above the burst height (*red circles*). *Black circles* show alternate scaling factors obtained for each spectrum by using the MLS climatology over all altitude ranges, instead of the ozonesonde profile. *Green dash lines* indicate the times of the change in the instrumentation described in Table 1

Ohyama *et al. Earth, Planets and Space* (2016) 68:34

Page 7 of 14

applied to the O_3 retrieval from space-borne spectra in the thermal infrared region, and it was expanded to the millimeter-wave region. In general, the relationship between the measurement vector **y** (measured spectrum) and the state vector **x** to be retrieved can be expressed by a nonlinear forward model **F** describing the radiative transfer in the atmosphere:

$$\mathbf{y} = \mathbf{F}(\mathbf{x}, \mathbf{b}) + \boldsymbol{\varepsilon}, \tag{3}$$

where **b** is the additional not-retrieved state vector and **ε** the measurement error vector. An optimal solution of **x** can be determined by minimizing the following cost function:

$$\begin{aligned} J(\mathbf{x})^2 = {}& [\mathbf{y} - \mathbf{F}(\mathbf{x}, \mathbf{b})]^T \mathbf{S}_{\boldsymbol{\varepsilon}}^{-1}[\mathbf{y} - \mathbf{F}(\mathbf{x}, \mathbf{b})] \\ & + (\mathbf{x} - \mathbf{x_a})^{\mathbf{T}} \mathbf{S}_{\mathbf{a}}^{-1}(\mathbf{x} - \mathbf{x_a}), \end{aligned} \tag{4}$$

where $\mathbf{x_a}$ is the a priori of **x**, $\mathbf{S_a}$ the a priori covariance matrix of $\mathbf{x_a}$, and $\mathbf{S_\varepsilon}$ the measurement covariance matrix associated with **y**. The retrieval algorithm gives the solution using the Levenberg–Marquardt method, whose general form is:

$$\begin{aligned} \mathbf{x}_{i+1} = {}& \mathbf{x}_i + \left[\mathbf{K}_i^{\mathbf{T}} \mathbf{S}_{\boldsymbol{\varepsilon}}^{-1} \mathbf{K}_i + (1 + \lambda_i) \mathbf{S_a} \right]^{-1} \\ & \left\{ \mathbf{K}_i^{\mathbf{T}} \mathbf{S}_{\boldsymbol{\varepsilon}}^{-1}[\mathbf{y} - \mathbf{F}(\mathbf{x}_i, \mathbf{b_a})] - \mathbf{S_a}^{-1}(\mathbf{x}_i - \mathbf{x_a}) \right\}, \end{aligned} \tag{5}$$

where index i is iteration number, $\mathbf{K}_i$ $(=\partial \mathbf{F}/\partial \mathbf{x}_i)$ is the Jacobian matrix of the forward model **F** with respect to $\mathbf{x}_i$, and λ_i is the Levenberg–Marquardt parameter whose value is chosen at each iteration step to minimize the cost function.

The input parameters to the forward model are the same as those used in deriving the scaling factor, but we used the daytime or nighttime MLS O_3 climatology over all altitudes as the a priori profile according to SZA. The daytime profile was used for the data whose SZA was below 98°. The a priori covariance matrix $\mathbf{S_a}$ and the measurement covariance matrix $\mathbf{S_\varepsilon}$ were set up as follows. The a priori uncertainties (square roots of the diagonal elements of $\mathbf{S_a}$) of the O_3 profile were assumed to be 30 % of the mixing ratios at each altitude. The uncertainty was estimated from the variability (deviation from the 30-day average) of O_3 mixing ratio in the stratosphere in a short term (Nagahama et al. 2004). The off-diagonal elements of the a priori covariance matrix were set to decrease exponentially with a correlation length of 6 km. The a priori uncertainties in the baseline polynomial and also the wavenumber shift were set to an extremely large value (i.e., 10^{10}), which represents no constraint to the a priori values. The measurement covariance matrix was assumed to be a diagonal matrix with elements corresponding to the brightness temperature noise levels of 0.35, 0.50, and 0.55 K for the periods before September 2005, between October 2005 and December 14, 2013, and after December 15, 2013, respectively.

Results and discussion

Data screening

In order to select the data that were not affected by thick cloud, we set the following condition: N_{ave} has to be equal to N_{total}, where N_{ave} is the number of spectra employed for calculating the hourly averaged spectrum based on the criteria described in the previous section and N_{total} is the total number of spectra measured within 1 h. In addition, the retrieval results that had a >0.15 K root-mean-square (RMS) residual between the observed and the calculated spectra were rejected. If the ratio of the two scaling factors (climatology/sonde), as shown in Fig. 3, did not range between 0.8 and 1.2, the retrieval results were screened out. Figure 4a shows an example of the spectral fit for the O_3 retrieval from the AOS-measured spectrum. The residual is equivalent to the spectral noise level, and the RMS residual is 0.04 K. Figure 4b presents the case of O_3 retrieval from the digital FFTS-measured spectrum, and the RMS residual is 0.08 K.

Figure 5 shows time series of the O_3 mixing ratio profiles between the altitudes of 20 and 60 km derived from the MWR measurements during the period from November 1999 to May 2014. The wet weather condition during the summer seasons interfered the MWR observations; specifically, the tropospheric opacities of more than 0.4 were frequently observed, and furthermore, the elevation angle of sky spectrum, which was automatically adjusted, reached the limited-angle. The seasonal cycle is different height by height. It shifts from summer maximum in the middle stratosphere (~35 km) to winter maximum in the upper stratosphere and the lower mesosphere (~45–55 km). During winter months, the O_3 mixing ratio in the upper stratosphere might be more variable than during the other seasons because sudden stratospheric warming induces large variability of O_3 (Flury et al. 2009) and the polar vortex occasionally moves toward mid-latitudes (Nagahama et al. 2007).
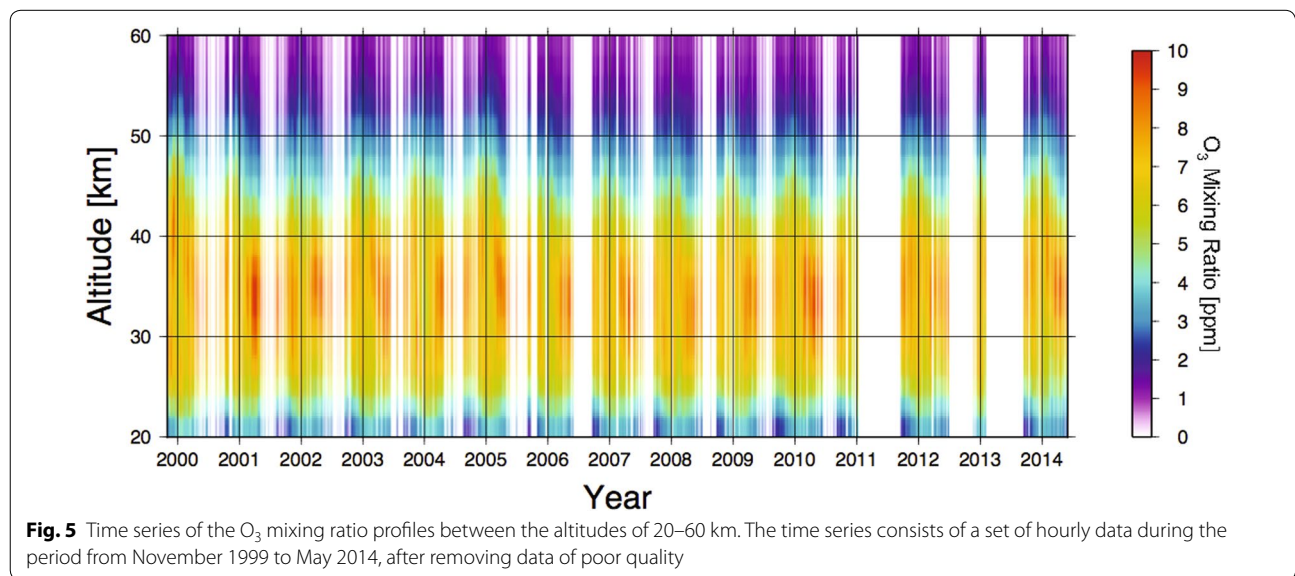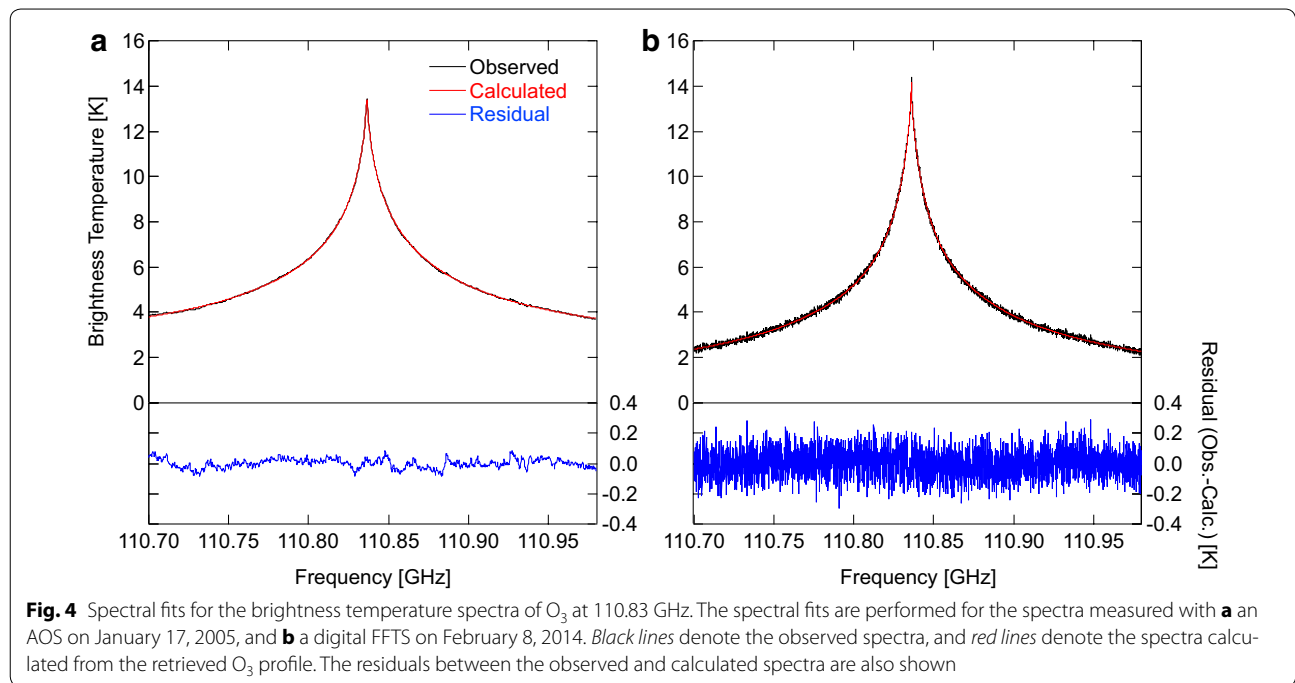
Error analysis

By introducing the gain matrix **G**, which indicates the sensitivity of the retrieved vector to the measurement:

$$\mathbf{G} = (\mathbf{K}^{\mathbf{T}} \mathbf{S}_{\boldsymbol{\varepsilon}}^{-1} \mathbf{K} + \mathbf{S_a})^{-1} \mathbf{K}^{\mathbf{T}} \mathbf{S}_{\boldsymbol{\varepsilon}}^{-1}, \tag{6}$$

the averaging kernel matrix **A** was represented by the product of **G** and the Jacobian matrix **K** at the last step of the iteration process (Rodgers 2000):

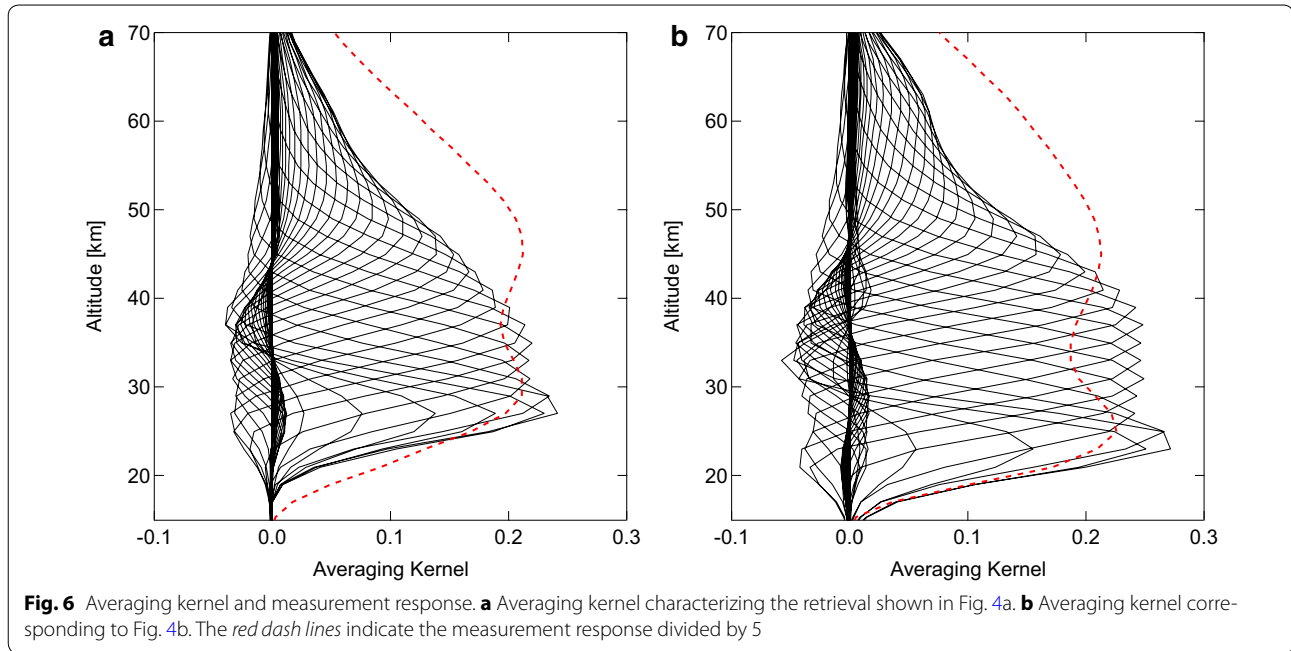$$\mathbf{A} = \mathbf{G}\mathbf{K} = \frac{\partial \hat{\mathbf{x}}}{\partial \mathbf{x}}. \tag{7}$$

Ohyama *et al. Earth, Planets and Space* (2016) 68:34

Page 8 of 14

Fig. 4 Spectral fits for the brightness temperature spectra of O_3 at 110.83 GHz. The spectral fits are performed for the spectra measured with **a** an AOS on January 17, 2005, and **b** a digital FFTS on February 8, 2014. *Black lines* denote the observed spectra, and *red lines* denote the spectra calculated from the retrieved O_3 profile. The residuals between the observed and calculated spectra are also shown

Fig. 5 Time series of the O_3 mixing ratio profiles between the altitudes of 20–60 km. The time series consists of a set of hourly data during the period from November 1999 to May 2014, after removing data of poor quality

The matrix **A** represents the sensitivity of the retrieved state $\hat{x}$ to the "true" state **x**, and each row of **A** indicates the vertical resolution of the measurements (Rodgers 2000). Figure 6a presents the averaging kernel that corresponds to the retrieval from the AOS-measured spectrum shown in Fig. 4a. The measurement response, which was calculated as the sum of the rows of averaging kernel (Rodgers 2000), is also shown in Fig. 6a. The retrieval has sensitivity in the altitude range, where the measurement response takes the values of more than 0.8. Therefore, Fig. 6a indicates that the O_3 retrieval has

sensitivity between ~24 and 56 km. Figure 6b presents the averaging kernel for the retrieval from the digital FFTS-measured spectrum shown in Fig. 4b, and the O_3 retrieval has sensitivity between ~21 and 58 km due to higher spectral resolution of the digital FFTS. The vertical resolution ranges from 7 to 10 km in the stratosphere and increases gradually to approximately 15–18 km at an altitude of 60 km.

The error sources expected in the analysis are presented here, and their effects on the O_3 retrieval are evaluated. The temporal variations of measured spectral

Ohyama *et al. Earth, Planets and Space* (2016) 68:34

Page 9 of 14

Fig. 6 Averaging kernel and measurement response. **a** Averaging kernel characterizing the retrieval shown in Fig. 4a. **b** Averaging kernel corresponding to Fig. 4b. The *red dash lines* indicate the measurement response divided by 5

intensity and tropospheric opacity, which are attributed to the instrumental problems, caused systematic error in the O_3 retrieval. However, because the measured spectral intensity and tropospheric opacity were corrected using the sonde data to the extent possible, we considered the systematic error to be negligible and take into account random error in what follows.

The linear error analysis for the retrieval was performed according to the formalism of Rodgers (2000) and Rodgers and Connor (2003), and the error covariance matrix was calculated for the individual retrieval process. The retrieval error can be represented by the difference between the retrieved state vector $\hat{\mathbf{x}}$ and the true state vector $\mathbf{x}$, and the analytical error can be estimated as below:

$$\hat{\mathbf{x}} - \mathbf{x} = (\mathbf{A} - \mathbf{I})(\mathbf{x} - \mathbf{x_a}) + \mathbf{G}\mathbf{K_b}(\mathbf{b} - \mathbf{b_a}) + \mathbf{G}\boldsymbol{\varepsilon}, \quad (8)$$

where $\mathbf{K_b}$ ($=\partial \mathbf{F}/\partial \mathbf{b}$) is the Jacobian matrix of the forward model $\mathbf{F}$ with respect to the non-retrieved model parameters $\mathbf{b}$ and $\mathbf{b_a}$ is the estimate of $\mathbf{b}$. $(\mathbf{A} - \mathbf{I})(\mathbf{x} - \mathbf{x_a})$ is called the smoothing error, $\mathbf{G}\mathbf{K_b}(\mathbf{b} - \mathbf{b_a})$ is the model parameter error, and $\mathbf{G}\boldsymbol{\varepsilon}$ is the measurement error. These three error sources in the retrieved O_3 profile are discussed in this section.

The smoothing error is the error resulting from the finite vertical resolution of the measurement. The smoothing error covariance $\mathbf{S_s}$ can be calculated from the following equation:

$$\mathbf{S_s} = (\mathbf{A} - \mathbf{I})\mathbf{S_c}(\mathbf{A} - \mathbf{I})^{\mathbf{T}}, \quad (9)$$

where $\mathbf{S_c}$ is the ensemble covariance matrix for the O_3 profile, which is here regarded as the same as the matrix $\mathbf{S_a}$.

The uncertainties in the input parameters into the forward model cause the model parameter error. The temperature profile, scaling factor, and tropospheric opacity that are fixed (not-retrieved) in the O_3 profile retrieval contribute to the model parameter error. The model parameter error covariance $\mathbf{S_f}$ is given by

$$\mathbf{S_f} = \mathbf{G}\mathbf{K_b}\mathbf{S_b}\mathbf{K_b^T}\mathbf{G^T}, \quad (10)$$

where $\mathbf{S_b}$ is the ensemble covariance matrix constructed from the uncertainties (1σ) in the model parameters: 6.7 % for scaling factor, 18 % for tropospheric opacity, and 10 K for temperature profile at each level. These uncertainties were estimated as follows. The uncertainty in the scaling factor was based on the value estimated above (±20 % at 3σ). The uncertainty in the tropospheric opacity was estimated from uncertainties in both the opacity calculated from sonde data and the opacity measured by the MWR. The uncertainty in the opacity calculated from sonde data was considered to be able to estimate from the monthly standard deviations of the percentage differences between the opacities calculated from the Nemuro and Sapporo sonde data, since the standard deviation would include the sonde data own measurement error and the effects of change of the sonde site as well as of spatial difference between the MWR and sonde sites; the average value was ~13 %. On the other hand, the uncertainty in the opacity measurement by the MWR was estimated to be ~12 % in Kuwahara et al. (2012). The overall uncertainty was taken as the square roots of the sum of the squares of the two uncertainties that was ~18 %.

Ohyama *et al. Earth, Planets and Space* (2016) 68:34

Page 10 of 14

Then, from lidar observation of atmospheric temperature over Tsukuba, Japan (Nakane et al. 1992), the differences between the observed temperature and climatology were up to 20 K in the stratosphere and 30 K in the mesosphere. Although the exact evaluation of the uncertainty in temperature used in the present study (NCEP reanalysis data up to approximately 30 km and CIRA climatology above) is difficult, we roughly estimated the uncertainty in temperature to be 10 K (1σ).

The measurement error is the error due to the spectral noise. The measurement error covariance $\mathbf{S_m}$ is represented by

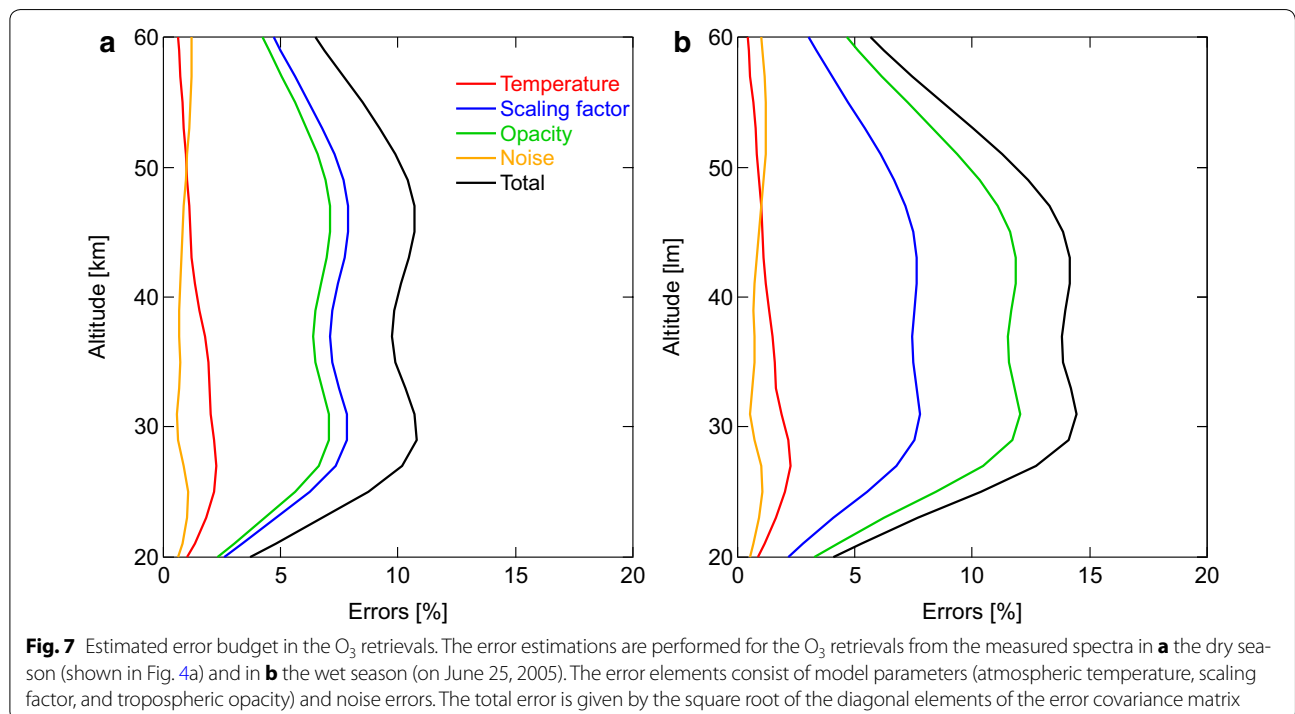$$\mathbf{S_m} = \mathbf{G}\mathbf{S_d}\mathbf{G^T}, \tag{11}$$

where $\mathbf{S_d}$ is taken to be a diagonal matrix with elements consisting of the square of the expected noise level in brightness temperature.
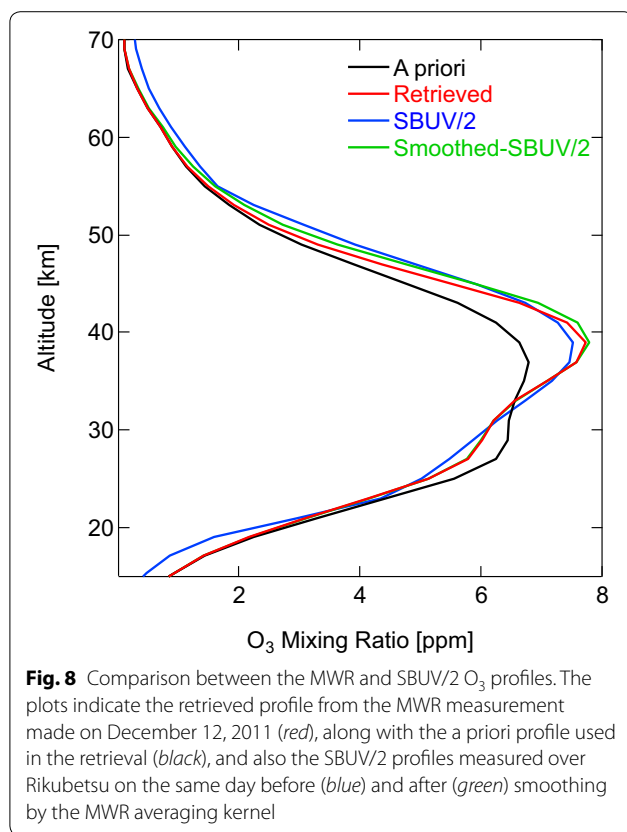
Figure 7 shows the error budget for the retrieved O_3 profiles. The total errors were taken as the square roots of the diagonal values of the total error covariance that corresponds to the sum of Eqs. 10 and 11. In our study, the smoothing error was not included in the total error estimate, but the retrieved O_3 profile is considered to be a smoothed representation of the true O_3 profiles. Alternatively, when the retrieved O_3 profile is compared with data having a higher vertical resolution (i.e., limb-viewing satellite data in this study), the smoothing error is accounted for by smoothing the higher-resolution profile

with the MWR averaging kernel, as described in the next subsection. The main contribution to the total error is the errors introduced by the uncertainties in the scaling factor and tropospheric opacity, followed by the spectral noise and atmospheric temperature errors. We found that the estimated total error for the dry season (Fig. 7a) ranged from 4 to 11 % in the altitude range of 20–60 km. In the case of the wet season (Fig. 7b), the estimated total error was partly larger than that of the dry season due to the larger error from the tropospheric opacity.

Validation using O_3 mixing ratios from satellite instruments

The retrieved O_3 profiles were compared with the SBUV/2 version 8.6 O_3 profile (Bhartia et al. 2013), the SABER version 2.0 O_3 profile (http://saber.gats-inc.com/data.php), and also the MLS version 3.3 or 3.4 O_3 profiles (Livesey et al. 2011). The orbits of the NOAA satellites carrying the SBUV/2 instruments gradually drift, which leads to shift of the equator crossing time. Kramarova et al. (2013) mentioned that the precision of SBUV/2 data becomes worse when the satellite is in a near-terminator orbit. We therefore used only the SBUV/2 data obtained within the equator crossing time of 8 A.M. to 4 P.M., namely the NOAA 11 data for the period of November 1999 to September 2000; the NOAA 16 data for the period of October 2000 to June 2007; and the NOAA 18 data for the period of July 2007 to November 2012. Kramarova

Fig. 7 Estimated error budget in the O_3 retrievals. The error estimations are performed for the O_3 retrievals from the measured spectra in **a** the dry season (shown in Fig. 4a) and in **b** the wet season (on June 25, 2005). The error elements consist of model parameters (atmospheric temperature, scaling factor, and tropospheric opacity) and noise errors. The total error is given by the square root of the diagonal elements of the error covariance matrix

Ohyama *et al. Earth, Planets and Space* (2016) 68:34

Page 11 of 14

Fig. 8 Comparison between the MWR and SBUV/2 O_3 profiles. The plots indicate the retrieved profile from the MWR measurement made on December 12, 2011 (*red*), along with the a priori profile used in the retrieval (*black*), and also the SBUV/2 profiles measured over Rikubetsu on the same day before (*blue*) and after (*green*) smoothing by the MWR averaging kernel

et al. (2013) also reported that (1) the SBUV/2 O_3 profiles among each satellite is in agreement within 10 % and (2) the SBUV/2 data in the lower stratosphere were smaller by up to 10 % than the MLS and other ground-based MWR data. As for SABER O_3 profile, Rong et al. (2009) indicated that the SABER version 1.07 (previous version) data have a systematic positive bias of 10–20 % from the middle stratosphere to the lower mesosphere, compared to other satellite data. Note that a thorough validation of the SABER version 2.0 data has not yet been published.

We set the spatial coincidence criteria so that the satellite data exist within a circle of 300-km radius around the Rikubetsu Observatory. The satellite data within the criteria for an overpass were averaged, and an MWR profile within ±30 min to the satellite data was picked out and compared to the satellite data. The numbers of SBUV/2, SABER, and MLS measurements that fulfilled the criteria are 318, 837, and 491, respectively. Because their satellite instruments look toward the edge of the atmosphere tangentially to the Earth's surface, the satellite profiles have much higher vertical resolution than the MWR profiles. For the sake of accurate comparison of the MWR measurement with the satellite measurement, we compared the MWR O_3 profile with the satellite O_3

profile smoothed by the MWR averaging kernels according to Eq. (12):

$$\hat{\mathbf{x}}_{\text{satellite}} = \mathbf{x_a} + \mathbf{A}(\mathbf{x}_{\text{satellite}} - \mathbf{x_a}), \qquad (12)$$

where $\hat{\mathbf{x}}_{\text{satellite}}$ and $\mathbf{x}_{\text{satellite}}$ are the smoothed and original satellite profiles, respectively. Figure 8 shows an example of the comparison of the MWR O_3 profile with the SBUV/2 O_3 profiles.

The time series of the O_3 mixing ratios derived from the MWR, SBUV/2, SABER, and MLS measurements at altitudes of 55, 45, 35, and 25 km are shown in Fig. 9a–d. The MWR O_3 mixing ratios at all altitudes reproduce well the seasonal and annual variations of the satellite data. Figure 10a shows mean differences in percent between the MWR profile and the satellite profile with the MWR averaging kernel applied; the difference was defined as the MWR minus satellite value. The standard deviations for the differences are shown in Fig. 10b. The results of the comparison reveal that the MWR O_3 retrievals are in good agreement with the MLS measurements: The mean difference is lower than ±5 % with a standard deviation of 4–9 % in the overall altitude range. The MWR O_3 profiles are negatively biased in the stratosphere and the lower mesosphere with respect to the SABER O_3 profiles. The mean difference is up to approximately 10 %, and its standard deviation ranges from 5 to 9 %. The large difference between the SABER and MWR can be explained by a systematic positive bias of 10–20 % for SABER O_3 mixing ratios from the middle stratosphere to the lower mesosphere (Rong et al. 2009). The standard deviation in the stratosphere indicates a value larger than that from the comparison between the MWR and MLS data. Compared to the SBUV/2 data, the MWR data in the lower stratosphere have a positive bias up to 10 % with a standard deviation of 5–8 %. This value is consistent with the result shown in Kramarova et al. (2013). Overall, after the systematic errors of the tropospheric opacity and the brightness temperature spectrum were corrected by the assistance of the sonde data and MLS climatological profiles, the retrieved O_3 profiles were in reasonable agreement with the satellite data with standard deviations of 5–10 %.
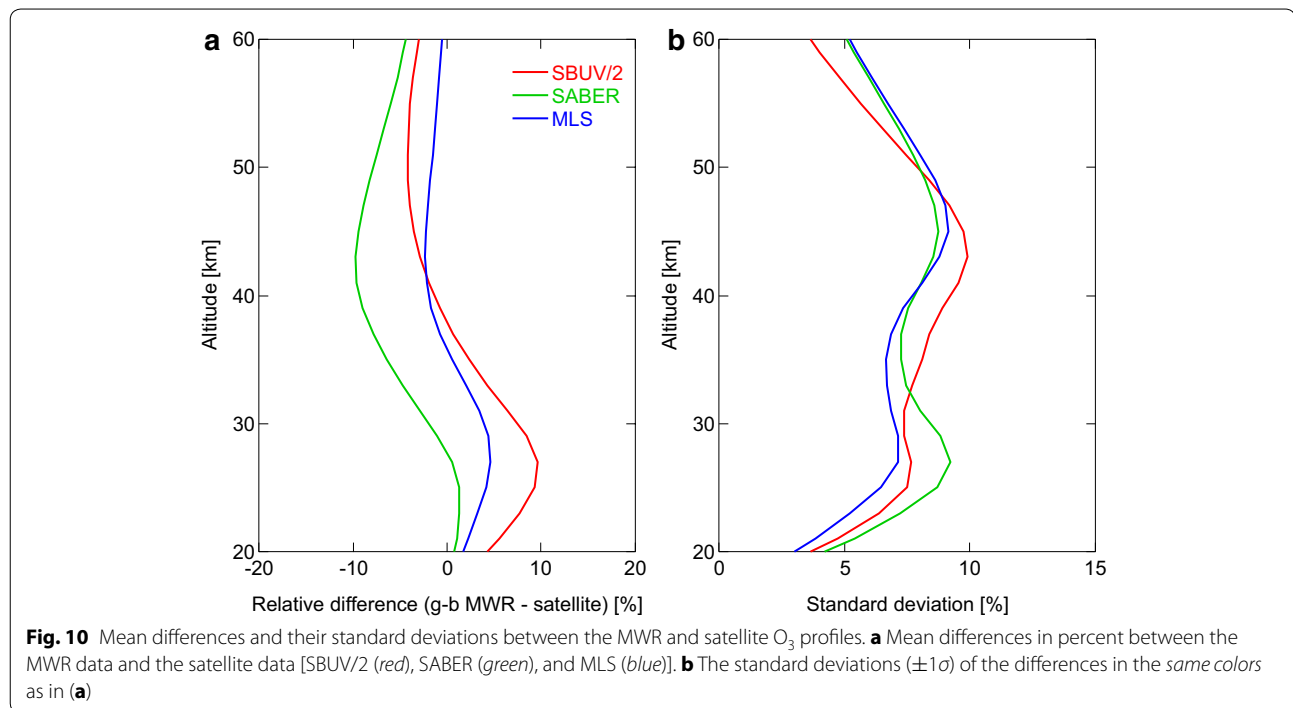
Conclusions

We have been monitoring vertical profiles of the O_3 mixing ratio in the stratosphere and mesosphere with the MWR installed at Rikubetsu, Japan, since November 1999. Replacements of the SIS receiver and spectrometer were carried out in 2005 and 2013. We found that the degradation of the SIS receiver and of the vessel for cold calibration load made the quality of the tropospheric opacity and spectral intensity worse. The tropospheric opacities were corrected using those calculated from the

Ohyama *et al. Earth, Planets and Space* (2016) 68:34

Page 12 of 14
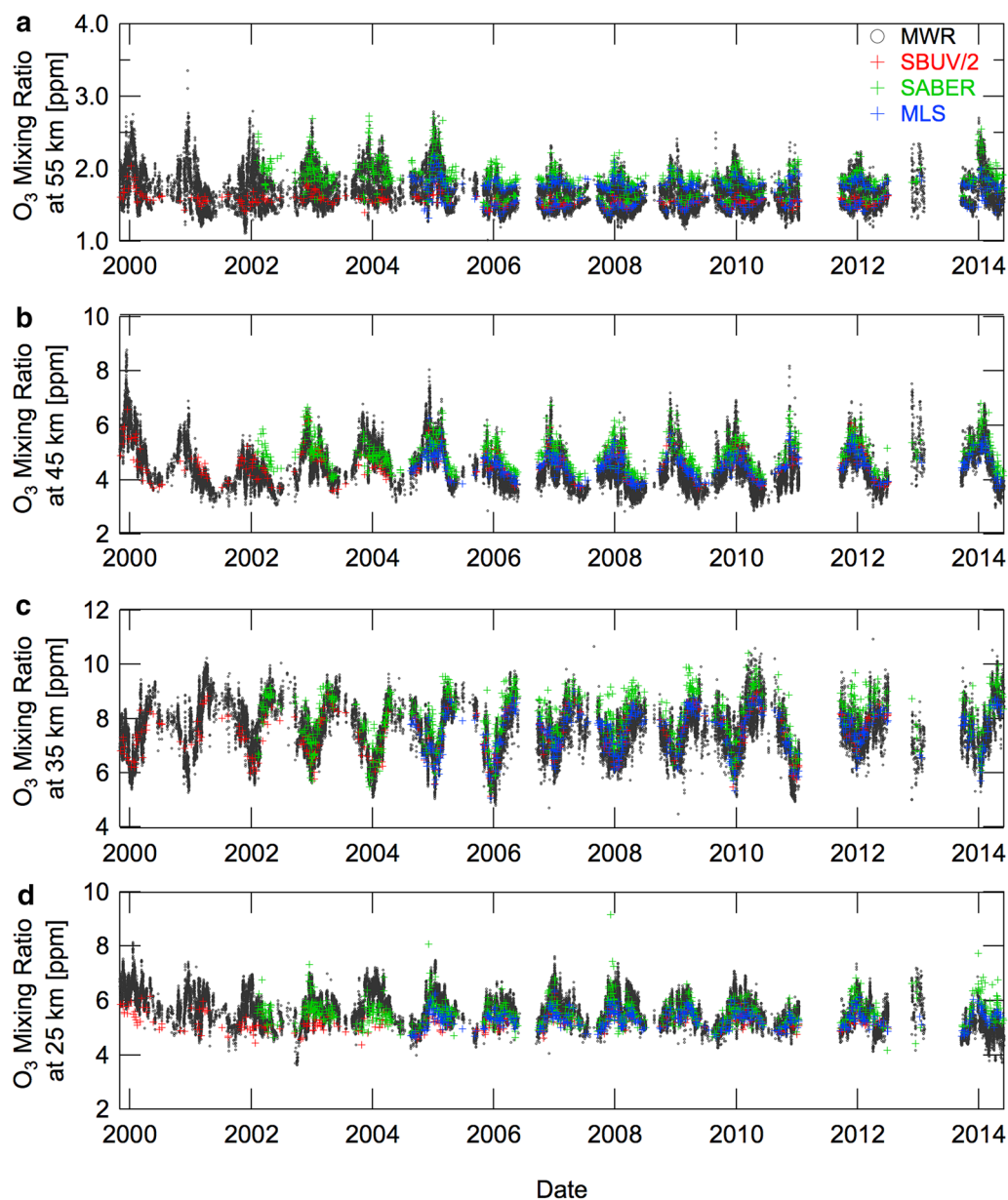
Fig. 9 Time series of the O_3 mixing ratios from the MWR and satellite measurements. The O_3 mixing ratios at altitudes of **a** 55, **b** 45, **c** 35, and **d** 25 km derived from the MWR (*black*), SBUV/2 (*red*), SABER (*green*), and MLS (*blue*) measurements are demonstrated

daily radiosonde profiles. The scaling factors for correcting the spectral intensity were derived using ozonesonde data and MLS monthly mean climatology. An analytical error evaluation was performed, and it was found that the retrieval errors resulting from uncertainties in the scaling factor and tropospheric opacity were dominant. The MWR O_3 mixing ratios between the altitudes of 24

and 56 km were compared with those derived from the space-based instruments (SBUV/2, SABER, and MLS). The MWR O_3 mixing ratios were negatively biased by ~10 % with a standard deviation of 5–9 % above 35 km compared to the SABER data, and were positively biased by ~10 % with a standard deviation of 5–8 % below 35 km compared to the SBUV/2 data. These biases were,

Ohyama *et al. Earth, Planets and Space* (2016) 68:34

Page 13 of 14

Fig. 10 Mean differences and their standard deviations between the MWR and satellite O_3 profiles. **a** Mean differences in percent between the MWR data and the satellite data [SBUV/2 (*red*), SABER (*green*), and MLS (*blue*)]. **b** The standard deviations (±1σ) of the differences in the *same colors* as in (**a**)

however, consistent with the validation results of the SABER and SBUV/2 data shown in the earlier literature. The comparison with the MLS data showed that the MWR O_3 mixing ratios at individual levels were on average consistent within ±5 % with a standard deviation of 4–9 %.

Abbreviations

AER: Atmospheric and Environmental Research; AOS: acousto-optical spectrometer; DSB: double sideband; FFTS: fast Fourier transform spectrometer; ISEE: Institute for Space-Earth Environmental Research; MLS: Microwave Limb Sounder; MWR: millimeter-wave radiometer; NIES: National Institute for Environmental Studies; OMI: Ozone Monitoring Instrument; RMS: root mean square; SABER: Sounding of the Atmosphere using Broadband Emission Radiometry; SBUV/2: Solar Backscatter Ultraviolet; SIS: superconductor–insulator–superconductor; SSB: single sideband; SZA: solar zenith angle; WOUDC: World Ozone and Ultraviolet Radiation Data Center.

Authors' contributions

HO (corresponding author) contributed to data analyses and preparation of the manuscript. TN, AM, HN, and HO (Hideo Ogawa) made contributions to the development of the millimeter-wave radiometer. All authors read and approved the final manuscript.

Author details

[1] Institute for Space-Earth Environmental Research, Nagoya University, Furo-cho, Chikusa-ku, Nagoya 464-8601, Japan. [2] Center for Global Environmental Research, National Institute for Environmental Studies, 16-2 Onogawa, Tsukuba, Ibaraki 305-8506, Japan. [3] Present Address: School of Environmental Science and Engineering, Kochi University of Technology, Tosayamada, Kami-City, Kochi 782-8502, Japan. [4] Department of Physical Science, Graduate School of Science, Osaka Prefecture University, 1-1 Gakuen-cho, Naka-ku, Sakai, Osaka 599-8531, Japan.

References

Asayama S, Ogawa H, Noguchi T, Suzuki K, Andoh H, Mizuno A (2004) An integrated sideband-separating SIS mixer based on waveguide split block for 100 GHz band with 4.0–8.0 GHz IF. Int J Infrared Millimeter Waves 25:107–117. doi:10.1023/B:IJIM.0000012766.63015.8c

Bhartia PK, McPeters RD, Flynn LE, Taylor S, Kramarova NA, Frith S, Fisher B, DeLand M (2013) Solar backscatter UV (SBUV) total ozone and profile algorithm. Atmos Meas Tech 6:2533–2548. doi:10.5194/amt-6-2533-2013

Daae M, Straub C, Espy PJ, Newnham DA (2014) Atmospheric ozone above Troll station, Antarctica observed by a ground based microwave radiometer. Earth Syst Sci Data 6:105–115. doi:10.5194/essd-6-105-2014

Durre I, Vose RS, Wertz DB (2006) Overview of the integrated global radiosonde archive. J Clim 19:53–68. doi:10.1175/JCLI3594.1

Ohyama *et al. Earth, Planets and Space* (2016) 68:34

Page 14 of 14

Fiorucci I, Muscari G, Froidevaux L, Santee ML (2013) Ground-based strato-spheric O_3 and HNO_3 measurements at Thule, Greenland: an intercom-parison with Aura MLS observations. Atmos Meas Tech 6:2441–2453. doi:10.5194/amt-6-2441-2013

Fleming EL, Chandra S, Barnett JJ, Corney M (1990) Zonal mean temperature, pressure, zonal wind and geopotential height as functions of latitude. Adv Space Res 10:11–59. doi:10.1016/0273-1177(90)90386-E

Flury T, Hocke K, Haefele A, Kämpfer N, Lehmann R (2009) Ozone depletion, water vapor increase, and PSC generation at midlatitudes by the 2008 major stratospheric warming. J Geophys Res 114:D18302. doi:10.1029/2009JD011940

Kalnay E, Kanamitsu M, Kistler R, Collins W, Deaven D, Gandin L, Iredell M, Saha S, White G, Woollen J, Zhu Y, Leetmaa A, Reynolds R, Chelliah M, Ebisuzaki W, Higgins W, Janowiak J, Mo KC, Ropelewski C, Wang J, Jenne R, Joseph D (1996) The NCEP/NCAR 40-year reanalysis project. B Am Meteorol Soc 77:437–471. doi:10.1175/1520-0477(1996)077<0437:TNYRP>2.0.CO;2

Kramarova NA, Frith SM, Bhartia PK, McPeters RD, Taylor SL, Fisher BL, Labow GJ, DeLand MT (2013) Validation of ozone monthly zonal mean profiles obtained from the version 8.6 Solar Backscatter Ultraviolet algorithm. Atmos Chem Phys 13:6887–6905. doi:10.5194/acp-13-6887-2013

Kuwahara T, Nagahama T, Maezawa H, Kojima Y, Yamamoto H, Okuda T, Mizuno N, Nakane H, Fukui Y, Mizuno A (2012) Ground-based millimeter-wave observation of stratospheric ClO over Atacama, Chile in the mid-latitude Southern Hemisphere. Atmos Meas Tech 5:2601–2611. doi:10.5194/amt-5-2601-2012

Livesey NJ, Read WG, Froidevaux L, Lambert A, Manney GL, Pumphrey HC, Santee ML, Schwartz MJ, Wang S, Cofield RE, Cuddy DT, Fuller R, Jarnot RF, Jiang JH, Knosp BW, Stek PC, Wagner PA, Wu DL (2011) EOS MLS Version 3.3 Level 2 data quality and description document. Technical report, Jet Propulsion Laboratory, D-33509. http://mls.jpl.nasa.gov

Mizuno A, Nagahama T, Morihira A, Ogawa H, Mizuno N, Yonekura Y, Yama-moto H, Nakane H, Fukui Y (2002) Millimeter-wave radiometer for the measurement of stratospheric ClO using a superconductive (SIS) receiver installed in the southern hemisphere. Int J Infrared Millimeter Waves 23:981–995. doi:10.1023/A:1019618917005

Mlawer EJ, Payne VH, Moncet JL, Delamere JS, Alvarado MJ, Tobin DC (2012) Development and recent evaluation of the MT_CKD model of continuum absorption. Philos Trans R Soc London A 370:2520–2556. doi:10.1098/rsta.2011.0295

Morris GA, Labow G, Akimoto H, Takigawa M, Fujiwara M, Hasebe F, Hirokawa J, Koide T (2013) On the use of the correction factor with Japanese ozonesonde data. Atmos Chem Phys 13:1243–1260. doi:10.5194/acp-13-1243-2013

Nagahama T, Nakane H, Fujinuma Y, Morihira A, Ogawa H, Mizuno A, Fukui Y (2004) Short-term variations of the stratospheric ozone measured with the ground-based millimeter-wave radiometer at Rikubetsu, Japan. In: Zerefos C (ed) Proceedings of the 20th quadrennial ozone symposium, Greece, June 2004

Nagahama T, Nakane H, Fujinuma Y, Morihira A, Mizuno A, Ogawa H, Fukui Y (2007) Ground-based millimeter-wave radiometer for measuring the stratospheric ozone over Rikubetsu, Japan. J Meteorol Soc Jpn 85:495–509. doi:10.2151/jmsj.85.495

Nakane H, Hayashida S, Sasano Y, Sugimoto N, Matsui I, Minato A (1992) Verti-cal profiles of temperature and ozone observed during DYANA campaign with the NIES ozone lidar system at Tsukuba. J Geomag Geoelectr 44:1071–1083. doi:10.5636/jgg.44.1071

Newchurch MJ, Yang ES, Cunnold DM, Reinsel GC, Zawodny JM, Russell JM III (2003) Evidence for slowdown in stratospheric ozone loss: first stage of ozone recovery. J Geophys Res 108:4507. doi:10.1029/2003JD003471

Ohyama H, Kawakami S, Shiomi K, Miyagawa K (2012) Retrievals of total and tropospheric ozone from GOSAT thermal infrared spectral radiances. IEEE Trans Geosci Remote 50:1770–1784. doi:10.1109/TGRS.2011.2170178

Palm M, Hoffmann CG, Golchert SHW, Notholt J (2010) The ground-based MW radiometer OZORAM on Spitsbergen—description and status of

stratospheric and mesospheric O_3-measurements. Atmos Meas Tech 3:1533–1545. doi:10.5194/amt-3-1533-2010

Parrish A, deZafra RL, Solomon PM, Barrett JW (1988) A ground-based tech-nique for millimeter wave spectroscopic observations of stratospheric trace constituents. Radio Sci 23:106–118. doi:10.1029/RS023i002p00106

Parrish A, Boyd IS, Nedoluha GE, Bhartia PK, Frith SM, Kramarova NA, Connor BJ, Bodeker GE, Froidevaux L, Shiotani M, Sakazaki T (2014) Diurnal variations of stratospheric ozone measured by ground-based microwave remote sensing at the Mauna Loa NDACC site: measurement validation and GEO-SCCM model comparison. Atmos Chem Phys 14:7255–7272. doi:10.5194/acp-14-7255-2014

Pickett HM, Poynter RL, Cohen EA, Delitsky ML, Pearson JC, Müller HSP (1998) Submillimeter, millimeter, and microwave spectral line catalog. J Quant Spectrosc Radiat Transf 60:883–890. doi:10.1016/S0022-4073(98)00091-0

Rodgers CD (2000) Inverse methods for atmospheric sounding: theory and practice. World Scientific, Singapore

Rodgers CD, Connor BJ (2003) Intercomparison of remote sounding instru-ments. J Geophys Res 108:4116. doi:10.1029/2002JD002299

Rong PP, Russell JM III, Mlynczak MG, Remsberg EE, Marshall BT, Gordley LL, López-Puertas M (2009) Validation of thermosphere ionosphere meso-sphere energetics and dynamics/sounding of the atmosphere using broadband emission radiometry (TIMED/SABER) v1.07 ozone at 9.6 μm in altitude range 15–70 km. J Geophys Res 114:D04306. doi:10.1029/2008JD010073

Rothman LS, Gordon IE, Babikov Y, Barbe A, Chris Benner D, Bernath PF, Birk M, Bizzocchi L, Boudon V, Brown LR, Campargue A, Chance K, Cohen EA, Coudert LH, Devi VM, Drouin BJ, Fayt A, Flaud J-M, Gamache RR, Harrison JJ, Hartmann J-M, Hill C, Hodges JT, Jacquemart D, Jolly A, Lamouroux J, Le Roy RJ, Li G, Long DA, Lyulin OM, Mackie CJ, Massie ST, Mikhailenko SN, Müller HSP, Naumenko OV, Nikitin AV, Orphal J, Perevalov VI, Perrin A, Polovtseva ER, Richard C, Smith MAH, Starikova E, Sung K, Tashkun SA, Tennyson J, Toon GC, VIG Tyuterev, Wagner G (2013) The HITRAN2012 molecular spectroscopic database. J Quant Spectrosc Radiat Transf 130:4–50. doi:10.1016/j.jqsrt.2013.07.002

Rowland FJ, Molina MJ (1975) Chloroflouromethanes in the environment. Rev Geophys 13:1–35. doi:10.1029/RG013i001p00001

Schneider N, Lezeaux O, de La Noë J, Urban J, Ricaud P (2003) Validation of ground-based observations of stratomesospheric ozone. J Geophys Res 108:4540. doi:10.1029/2002JD002925

Smit HGJ, Straeter W, Johnson B, Oltmans S, Davies J, Tarasick DW, Hoegger B, Stubi R, Schmidlin F, Northam T, Thompson A, Witte J, Boyd I, Posny F (2007) Assessment of the performance of ECC-ozonesondes under quasi-flight conditions in the 10 environmental simulation chamber: Insights from the Juelich Ozone Sonde Intercomparison Experiment (JOSIE). J Geophys Res 112:D19306. doi:10.1029/2006JD007308

Solomon S (1999) Stratospheric ozone depletion: a review of concepts and history. Rev Geophys 37:275–316. doi:10.1029/1999RG900008

Studer S, Hocke K, Kämpfer N (2012) Intraseasonal oscillations of strato-spheric ozone above Switzerland. J Atmos Sol-Terr Phys 74:189–198. doi:10.1016/j.jastp.2011.10.020

Tretyakov MY, Koshelev MA, Dorovskikh VV, Makarov DS, Rosen-kranz PW (2005) 60-GHz oxygen band: precise broadening and central frequen-cies of fine-structure lines, absolute absorption profile at atmospheric pressure, and revision of mixing coefficients. J Mol Spectrosc 231:1–14. doi:10.1016/j.jms.2004.11.011

Ulich BL, Davis JH, Rhodes PJ, Hollis J (1980) Absolute brightness temperature measurements at 3.5-mm wavelength. IEEE Trans Antennas Propag 28:367–376. doi:10.1109/TAP.1980.1142330

Van Vleck JH (1947) The absorption of microwaves by oxygen. Phys Rev 71:413–424. doi:10.1103/PhysRev.71.413

WMO (2014) Assessment for decision-makers: scientific assessment of ozone depletion: 2014. Global Ozone Research and Monitoring Project-report no. 56, Geneva, Switzerland